Molecular Catalysis 591 (2026) 115702

Contents lists available at ScienceDirect

Molecular Catalysis

journal homepage: www.journals.elsevier.com/molecular-catalysis

MOF-constrained Rh enables stable in situ H_2O_2 supply for peroxide-dependent enzymes

Yutong Wang [a,b,*], Chunyu Huang [c], Jelco Albertsma [c], Monique van der Veen [c], Miguel Alcalde [d], Frank Hollmann [a]

[a] Department of Biotechnology, Delft University of Technology, Van der Maasweg 9, 2629 HZ, Delft, the Netherlands
[b] Department of Chemical Engineering and Technology, Tianjin University, Yaguan Road 135, 300350, Tianjin, PR China
[c] Department of Chemical Engineering, Delft University of Technology, Van der Maasweg 9, 2629 HZ, Delft, the Netherlands
[d] Department of Biocatalysis, Institute of Catalysis, CSIC, 28049 Madrid, Spain

ARTICLE INFO

Keywords:
H_2O_2 generation
Rhodium
FMN reduction
UiO-67
Peroxygenase

ABSTRACT

Peroxide-dependent enzymes often suffer from irreversible oxidative deactivation by the peroxide co-substrate. Transition metal mediated in situ generation of H_2O_2 offers continuous peroxide feeding in low concentration. However, free metal complexes often interact non-selectively with proteins, leading to mutual deactivation of metal catalysts and enzymes. Here, we report a spatial isolation strategy using zirconium-based metal-organic frameworks (UiO-67) to immobilize the transition metal catalytic unit [Cp*Rh(bpy)Cl]$^+$. The porous MOF structure acts as a molecular sieve, excluding enzymes from the Rh sites on the framework, thus protecting both catalysts from mutual deactivation. The Rh modified UiO-67 (Rh@UiO-67) catalyzes the flavin-mediated electron transfer from formate to oxygen, generating H_2O_2 in a formate oxidase mimicking fashion. Its protein compatibility allows Rh@UiO-67 to fuel peroxyzymes for stable oxyfunctionalization. Compared to natural formate oxidase, this system also shows high stability to various pH and temperatures, enabling its application in versatile conditions.

1. Introduction

The organometallic complex $[Cp^*Rh(bpy)(H_2O)]^{2+}$ has been investigated for over three decades as a versatile, non-enzymatic catalyst for the regeneration of enzymatic cofactors [1] Its particular strength lies in its broad substrate scope: unlike many classical enzymatic systems, $[Cp^*Rh(bpy)(H_2O)]^{2+}$ does not discriminate between phosphorylated (NADP) and non-phosphorylated (NAD) nicotinamide cofactors, can regenerate both oxidised (NAD(P)$^+$) and reduced (NAD(P)H) forms, and also shows significant activity towards other biological cofactors such as flavins (FAD, FMN, riboflavin) [2] and even heme [3]

Furthermore, the catalytically active species $[Cp^*Rh(bpy)H]^+$ can be generated using a wide range of stoichiometric reductants, including photochemical and electrochemical sources, [1d] formate [4] or phosphite [5] More recently, analogous iridium complexes have been applied to generate H_2O_2 to promote peroxygenase-catalyzed oxyfunctionalization reactions [6]

One of the main challenges in combining transition-metal complexes with enzymes, however, is their frequently observed mutual inactivation. We hypothesized that this inactivation may arise from the coordination of the rhodium center to nucleophilic amino acid residues in the biocatalyst, such as histidine and cysteine, which lead to irreversible denaturation (Scheme S1) [7] Such strong binding would impair the coordinative interaction of formate or phosphite, thereby inactivating $[Cp^*Rh(bpy)]^{2+}$. Conversely, this coordination may also interfere with catalytically relevant interactions within the enzyme and/or compromise its structural integrity.

One possible solution is the physical separation to restrict the interactions between enzyme and organometallic complex, for example in an enzyme-membrane reactor (Scheme 1) [8] However, catalyst performance in this configuration was unsatisfactory, possibly owing to diffusion limitations. Another strategy to prevent undesired interactions between the rhodium center and the biocatalyst is to introduce steric protection. Ward's biotin/streptavidin technology has shown some promise in this regard [9]

Porous materials such as mesoporous silica [11] and, more powerfully, microporous metal-organic frameworks (MOFs) [12] can function as molecular sieves, excluding large biomolecules while allowing better

* Corresponding author.
E-mail address: y.wang-37@tudelft.nl (Y. Wang).

https://doi.org/10.1016/j.mcat.2026.115702
Received 7 December 2025; Received in revised form 31 December 2025; Accepted 3 January 2026
Available online 8 January 2026

diffusion of smaller substrates and cofactors given their pore apertures. Among these, the zirconium-based MOF UiO-67 offers an attractive scaffold owing to its exceptional stability. Structurally, UiO-67 is composed of Zr-oxoclusters ($[Zr_6^{IV}O_4(OH)_4]^{12+}$) nodes and biphenyl-4, 4′-dicarboxylate (BPDC) linkers [13] Although UiO-67 derivatives possess two types of cages with diameters of 11 Å and 23 Å which allows efficient substrate or cofactor transportation, its window size of 8 Å restricts access of bulky molecules [14] For example, UiO-67 framework could efficiently encapsulate heterogeneous catalyst with diameter of 12 Å [15] Therefore, UiO-67 imposed size-exclusion to most of the enzymes (a globular protein of 10 kDa has an approximate diameter of 10 Å). This spatial separation completely prevents metal coordination within the enzyme and substantially limits enzyme-metal interactions at the interface, thereby preserving the catalytic structures of both the enzyme and the metal sites.

To test our hypothesis, we employed the formate/$[Cp^*Rh(bpy)]^{2+}$/flavin/O_2 system, in which formate serves as the stoichiometric reductant for $[Cp^*Rh(bpy)]^{2+}$, generating the hydride species $[Cp^*Rh(bpy)H]^{+}$. This hydride then transfers electrons to the flavin cofactor, which in turn reduces molecular oxygen to hydrogen peroxide, thereby supplying the oxidant required for peroxygenase-catalyzed oxyfunctionalization reactions (Scheme 2).

2. Experiment section

2.1. Preparation of Rh@UiOs

UiO-67 and UiO-67-Bpy were synthesized by refluxing. 0.25 mmol (58.25 mg) of $ZrCl_4$ was firstly dissolved in 3.5 mL DMF and dispersed by stirring at 155°C for 30 min. 0.25 mmol (61.05 mg) of organic linker (H_2BPyDC or H_2BPDC) was dissolved in 7.5 mL DMF, sonicated, and mixed with 1.145 mL acetic acid to make linker stock solution. The linker solution was then added to the $ZrCl_4$ solution followed by refluxing at 155°C for 24 hours. The precipitate was collected by centrifuge at 12,000 rpm, washed with DMF and methanol three times each, and dried overnight at room temperature (20 °C) under vacuum.

[Cp*Rh(BPyDC)Cl]Cl was synthesized according to the literature with minor modifications [1,2] To 30 mL of methanol, 1 eq. (0.32 mmol) of $[Cp^*RhCl]_2Cl_2$ and 2 eq. (0.76 mmol) of H_2BPyDC was dissolved and stirred at room temperature for 24 hours in dark. The resulting orange-yellow solution was dried under vacuum. The residual was dissolved in a minimal quantity of methanol, followed by precipitation upon addition of diethyl ether. The yellow precipitate was collected and dried under vacuum. Structure of the product was confirmed by NMR (Fig S7).

Rh were incorporated to the UiO frameworks by post-synthesis linker exchange (PSE). 10 mg of UiO-67 or UiO-67-Bpy and various amount of [Cp*Rh(BPyDC)Cl]Cl were dispersed in 0.5 mL degassed water by sonication, and then stirred in dark for 24 hours. The resulting Rh@UiOs was collected by centrifuge at 12,000 rpm, washed with DMF once and isopropanol twice, and dried overnight at room temperature (20 °C) under vacuum.

2.2. Trans-hydrogenation by Rh@UiOs

Hydrogenation of cyclohexanone was performed in Tris-HCl buffer (25 mM, pH 8.0) contains 0.5 M formate, Rh catalyst (Rh@UiO 2 mg/mL or [Cp*Rh(BPyDC)Cl]Cl 0.2 mM), and cyclohex-2-enone 4 mM as the substrate. The reaction was stopped by extracting 100 μL reaction mixture with 250 μL ethyl acetate. The organic phase was analyzed by gas chromatography using phenol as an internal standard. The reactions were performed at 40°C, 800 rpm in 2 mL Eppendorf tubes. Hot filtration of the Rh@UiO was done with 0.22 μm syringe membrane filter.

Depletion of oxygen in its oxidation catalyzed by Rh@UiO/FMN was monitored by Clark electrode in a sealed chamber. The electrode was calibrated with air-saturated water and solution deoxygenated by sodium disulfite. The reaction in air-saturated Tris-HCl buffer (50 mM, pH 8.0) contains 0.1 M formate, Rh@UiO 0.25 mg/mL, and FMN 50 μM. The reaction was performed at r.t. (20°C) with continuous stirring.

The reduction of FMN was monitored by microplate reader in the glovebox, following the depletion of the FMN absorption band at 450 nm (ε=12500 M^{-1} cm^{-1}). The reactions in degassed Tris-HCl buffer (25 mM, pH 8.0) contains 0.3 M formate, 50 μM FMN, and 50 μg/mL Rh@UiO-67.

2.3. Rh@UiO-67/FMN-AaeUPO tandem reaction

The reactions were performed in Tris-HCl buffer (25 mM, pH 8.0) contains 0.4 M formate, Rh@UiO-67 (PSE 20%) 2 mg/mL, FMN 4 mM, and *Aae*UPO PaDa-I 1 μM. In monophasic aqueous system, reaction was started by adding 4 % (v/v) of 0.5 M ethylbenzene in acetonitrile, leading to final EB concentration of 20 mM. In biphasic system, the reaction was started by adding 10 % (v/v) of 0.5 M EB in ethyl acetate, which introduces the second phase. The reactions were performed in 1.5 mL glass vial at 40°C, 800 rpm. Reactions were stopped by extracting 50 μL reaction mixture with 250 uL (monophasic) or 240 uL (biphasic) EtOAc. The organic phase was analysed by gas chromatography using octanol as internal standard.

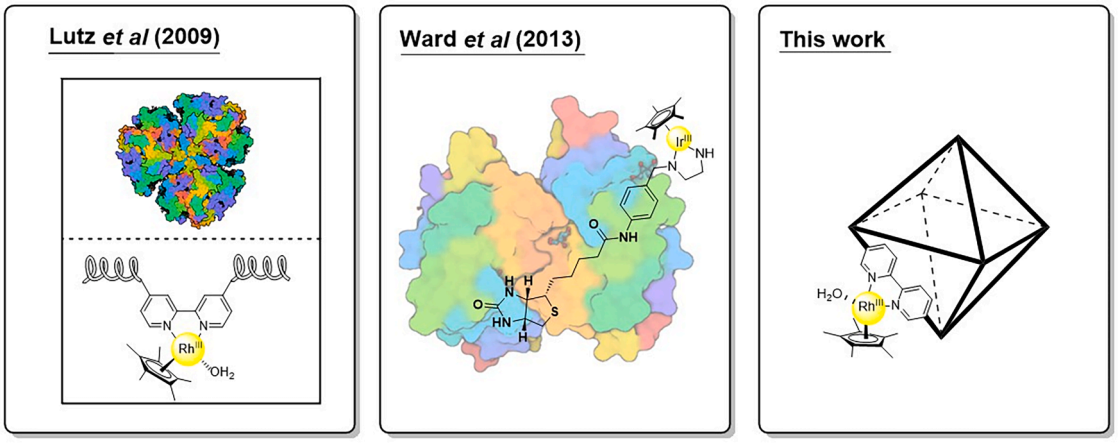

Scheme 1. Methods to mitigate the mutual inactivation of transition metal-based cofactor regeneration catalysts and enzymes. Lutz and co-workers employed polymer-modified $[Cp^*Rh(bpy)]^{2+}$ complexes, which could be separated from the biocatalyst using an ultrafiltration membrane [8] Ward and co-workers applied the biotin/streptavidin technology to position an iridium-based metal catalyst within a sterically demanding polypeptide environment [10] Here, we propose the immobilization of $[Cp^*Rh(bpy)]^{2+}$ on metal-organic frameworks (MOFs).

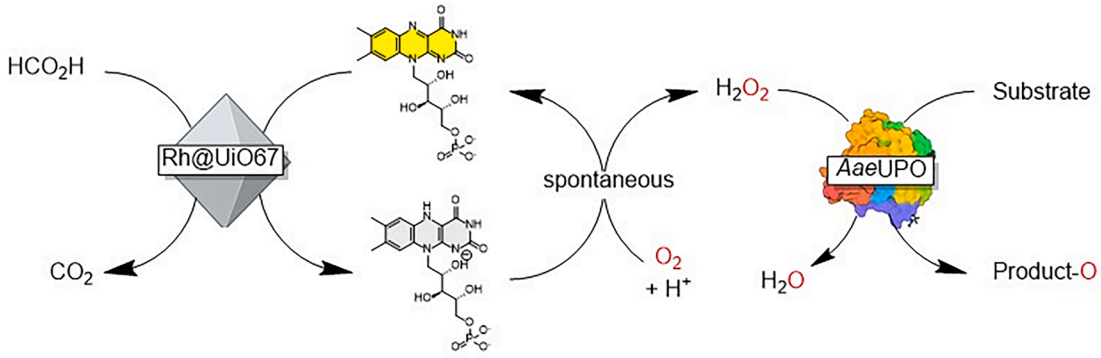

Scheme 2. Peroxygenase catalyzed oxyfunctionalization fueled by hydrogen peroxide generated by formate/$[Cp^*Rh(bpy)]^{2+}$/flavin/O_2 system. (Rh@UiO-67 represents the Rh active site modified on UiO-67 framework. Crystal structure of *Aae*UPO is used as model enzyme, PDB: 5OXU).

3. Result and discussion

3.1. Construction of Rh@UiOs

Our synthesis strategy was to utilize bipyridyl linkers (BPyDC) instead of the original BPDC linkers thereby generating coordination sites for the Cp*Rh unit. The resulting UiO-67-Bpy exhibited almost same XRD pattern and characteristic octahedral morphology as UiO-67 (Fig. 1b). However, treatment of UiO-67-Bpy with the $[Cp^*RhCl_2]_2$ catalyst precursor did not result in significant incorporation. We therefore applied post synthetic exchange (PSE) to replace the linkers within UiO-67 and UiO-67-Bpy with $[Cp^*Rh(BPyDC)]^{2+}$ linker (Fig. 1a), resulting in Rh@UiO-67 and Rh@UiO-67-Bpy, respectively [15] The powder X-ray diffraction patterns of both Rh@UiO-67 and Rh@UiO-67-Bpy remained consistent with those of the parent frameworks despite some loss in XRD-peak intensity (Fig. 2a), confirming that the crystallinity were mainly retained.

Upon incorporation of the Cp*Rh unit, Rh@UiO-67 showed partial morphological degradation, but the octahedral morphology was largely preserved (Fig. 2a). Elemental mapping confirmed uniform distribution of Zr and Rh over the particles, indicating successful incorporation of the Rh centers. In contrast, linker exchange of UiO-67-Bpy led to significant morphological changes, with the original octahedral crystals transforming into an amorphous morphology, probably resulting in more readily access of Rh-active sites (Fig. 2b). While some bulk particles remained, Rh was predominantly localized in the amorphous regions, suggesting that the morphology change of UiO-67-Bpy was related to the PSE process. Infrared spectra further showed that the characteristic bands of UiO-67, attributed to O-Zr vibrations and carboxylate-coordination with Zr clusters, were preserved after PSE (Fig. S1). A new weak band at 1365 cm^{-1} indicated the incorporation of bipyridine groups, accompanied by a 5 cm^{-1} blue shift in the 1592 cm^{-1} band, consistent with increased electron density on the carboxylate. UV-Vis spectroscopy revealed aromatic π-π* transitions at 278 nm in UiO-67 and its organic linker BPDC, while UiO-67-Bpy and BPyDC exhibited absorptions at 247 nm and 295 nm (Fig. 2c-d). Following PSE, new

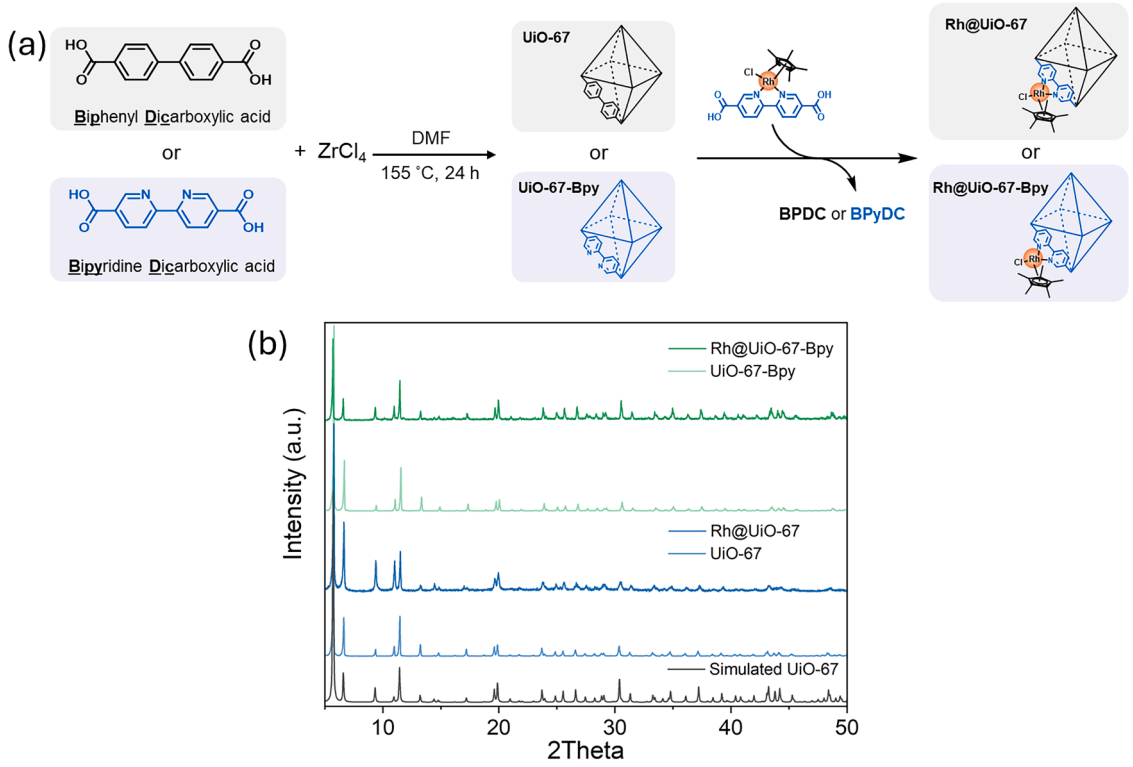

Fig. 1. (a) Scheme of MOF synthesis and PSE for incorporation of [Cp*Rh] catalytic sites. (b) PXRD patterns of crystallinity of UiO-67 and UiO-67-Bpy before and after PSE. (Dosing ratio of [Cp*Rh(BPyDC)Cl]Cl was 30 mol% based on the original linker content in ideal UiO-67).

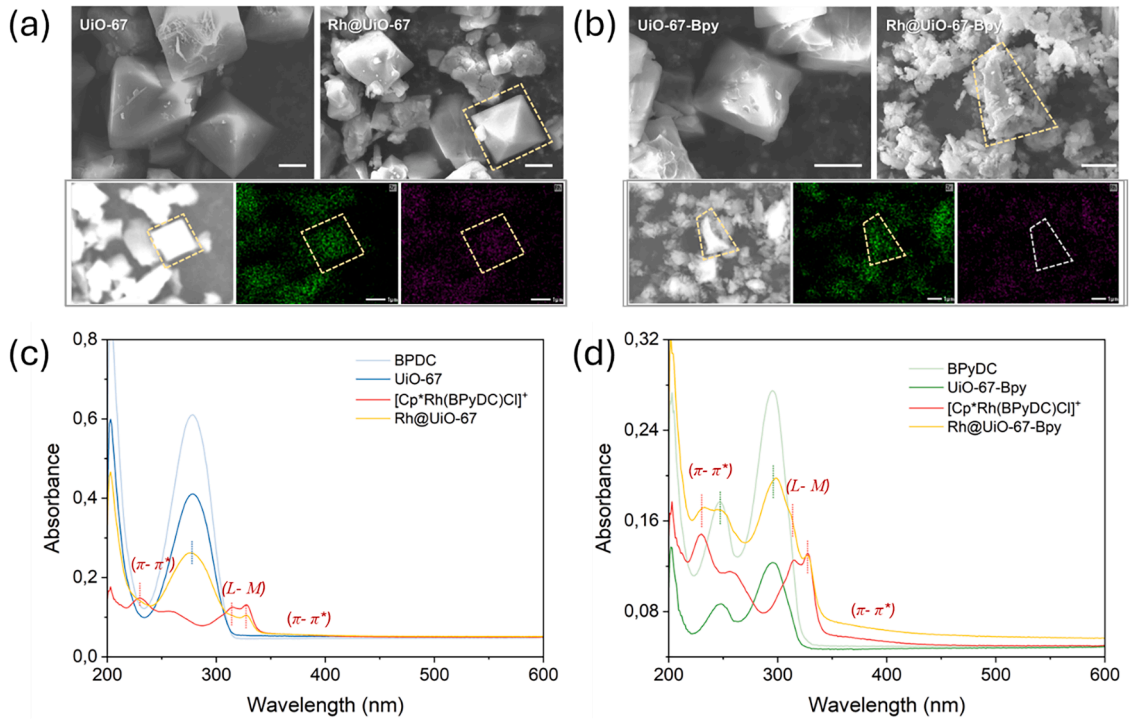

Fig. 2. Structural characterization of Rh@UiO-67 and Rh@UiO-67-Bpy. (a) SEM morphology characterization of UiO-67, Rh@UiO-67 (above), and EDX elementary analysis of Rh@UiO-67 (below). (b) SEM morphology characterization of UiO-67-Bpy, Rh@UiO-67-Bpy (above), and EDX elementary analysis of Rh@UiO-67-Bpy (below). (c-d) UV-Vis spectra of UiO-67 and UiO-67-Bpy before and after PSE. (Dosing ratio of [Cp*Rh(BPyDC)Cl]Cl was 30 mol% based on the original linker amount in ideal UiO-67. Green and violet dots in elemental mapping show the distribution of zirconium and rhodium, respectively. The scale bars are 1 μm.).

absorption features appeared at 230 nm, 314-327 nm, and 350-400 nm in both Rh@UiO-67 and Rh@UiO-67-Bpy, which can be assigned to π-π* transitions, ligand-to-metal charge transfer (LMCT), and Rh-based n-π* transitions, respectively, originating from the $[Cp^*Rh(BpyDC)Cl]^+$ complex.

X-ray photoelectron spectroscopy confirmed the presence of Rh and N from $[Cp^*Rh(BPyDC)]^{2+}$ in Rh@UiO-67 (Fig. S2). High resolution Rh-XPS indicated that the coordination status of $[Cp^*Rh(BPyDC)]^{2+}$ within Rh@UiO-67 was preserved relative to the free complex. Similar Rh-related peaks were observed in Rh@UiO-67-Bpy, while the C-N=C signal of the pre-existing bipyridine groups remained unchanged. Quantitative analysis of Rh loading was carried out by ICP-OES, EDX, and XPS (Table 1). At a 30 mol% $[Cp^*Rh(BPyDC)Cl]^+$ doping ratio during linker exchange, both Rh@UiO-67 and Rh@UiO-67-Bpy incorporated 1 wt% Rh according to ICP and EDX, corresponding to an atomic ratio of 0.15-0.19%. However, XPS detected significantly higher Rh contents (1.07-1.20% atomic), nearly six-times the bulk value. The higher Rh content observed by XPS suggests that the ligand exchange predominantly occurred on the surface. Similar Rh incorporation ratio was achieved in Rh@UiO-67 and Rh@UiO-67-Bpy when PSE ratio was applied.

Table 1
Rh analysis for different Rh-MOF species.

Method	Analysis range	Sample[a]	Mass ratio (%)	Atomic ratio (%)
ICP-OES	Bulk	Rh@UiO-67	1.0	0.14[b]
		Rh@UiO-67-Bpy	1.0	0.12[b]
EDX	Bulk	Rh@UiO-67	1.19	0.15
		Rh@UiO-67-Bpy	1.37	0.19
XPS	Surface	Rh@UiO-67		1.07
		Rh@UiO-67-Bpy		1.20
		[Cp*Rh(BpyDC)Cl]Cl		2.42[c]

[a] PSE was performed using an added [Cp*Rh(BPyDC)Cl]Cl amount corresponding to 30 mol% of the original MOF's linker content.
[b] Atomic ratio of Rh was estimated based on the mass ratio determined by ICP-OES, assuming no defects in the UiO-67.
[c] Theoretical atomic Rh content in [Cp*Rh(BpyDC)Cl]Cl linker is 2.7 %.

3.2. Catalytic activity of Rh@UiOs

To evaluate the catalytic activity of Rh@UiO-67 and Rh@UiO-67-Bpy in formate-driven reactions, we investigated both the reduction of cyclohex-2-enone and the targeted catalytic reduction of O_2 to H_2O_2.

In the case of cyclohexenone conversion, when Rh molar concentration was kept constant, the MOF-embedded $[Cp^*Rh(BPyDC)]^{2+}$ complexes exhibited higher catalytic activity than their homogeneous counterparts, $[Cp^*RhCl_2]_2$ and $[Cp^*Rh(BPyDC)Cl]^+$, despite that the activity of $[Cp^*Rh(BPyDC)Cl]^+$ increased with concentration (Fig. 3a). The molecular basis of the enhanced activity in the MOF-embedded system remains unclear, although it is conceivable that the Lewis acidity of the $[Zr^{IV}_6O_4(OH)_4]^{12+}$ nodes synergistically activate cyclohexenone towards Michael-type hydride attack [16] Further investigations will be required to substantiate this effect.

We next examined the selective reduction of O_2 to H_2O_2. To this end, we monitored O_2 depletion in the reaction medium under catalytic turnover conditions (Fig. 3b). Once again, both Rh@UiO-67 and Rh@UiO-67-Bpy exhibited significant catalytic activity, which correlated with the rhodium content of the MOF catalysts.

In both model reactions, Rh@UiO-67-Bpy consistently exhibited higher activity than Rh@UiO-67. This difference arises from multiple factors. First, PSE induced a structural transformation of Rh@UiO-67-Bpy into a lamellar-like nanostructure, thereby increasing the accessible surface area and shortening the mass transporting distance inside the particle. In contrast, Rh@UiO-67 maintained the octahedral cubic morphology from UiO-67, where greater mass transfer resistance could be expected, resulting in lower catalytic velocity (Fig. 2a-b). Second,

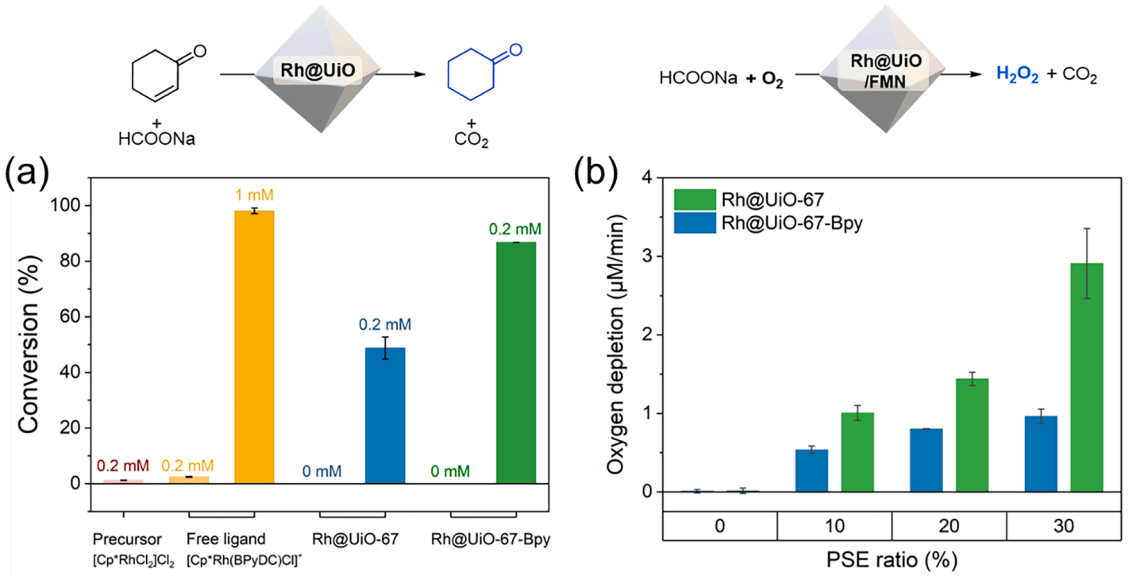

Fig. 3. Catalytic performance of Rh@UiO. (a) Hydrogenation of cyclohex-2-en-1-one. The reactions in Tris-HCl buffer (25 mM, pH 8.0) contains 0.5 M formate, Rh catalyst (Rh@UiO 2 mg/mL or free complexes 0.2-1 mM, the Rh-content in Rh@UiOs was modulated by changing doping ratio in PSE), and 4 mM cyclohexenone. (b) Oxygen depletion in the H_2O_2 generation catalyzed by Rh@UiO/FMN. The reaction in air-saturated Tris-HCl buffer (50 mM, pH 8.0) contains 0.1 M formate, Rh@UiO 0.25 mg/mL, and FMN 50 μM.

electronic environment of Cp*Rh also contributes. High-resolution XPS analysis revealed a positive shift in Rh^{III} binding energy upon incorporated into the MOFs (Fig. S3). This shift was more pronounced for Rh@UiO-67, indicating lower electron density at its Rh center.

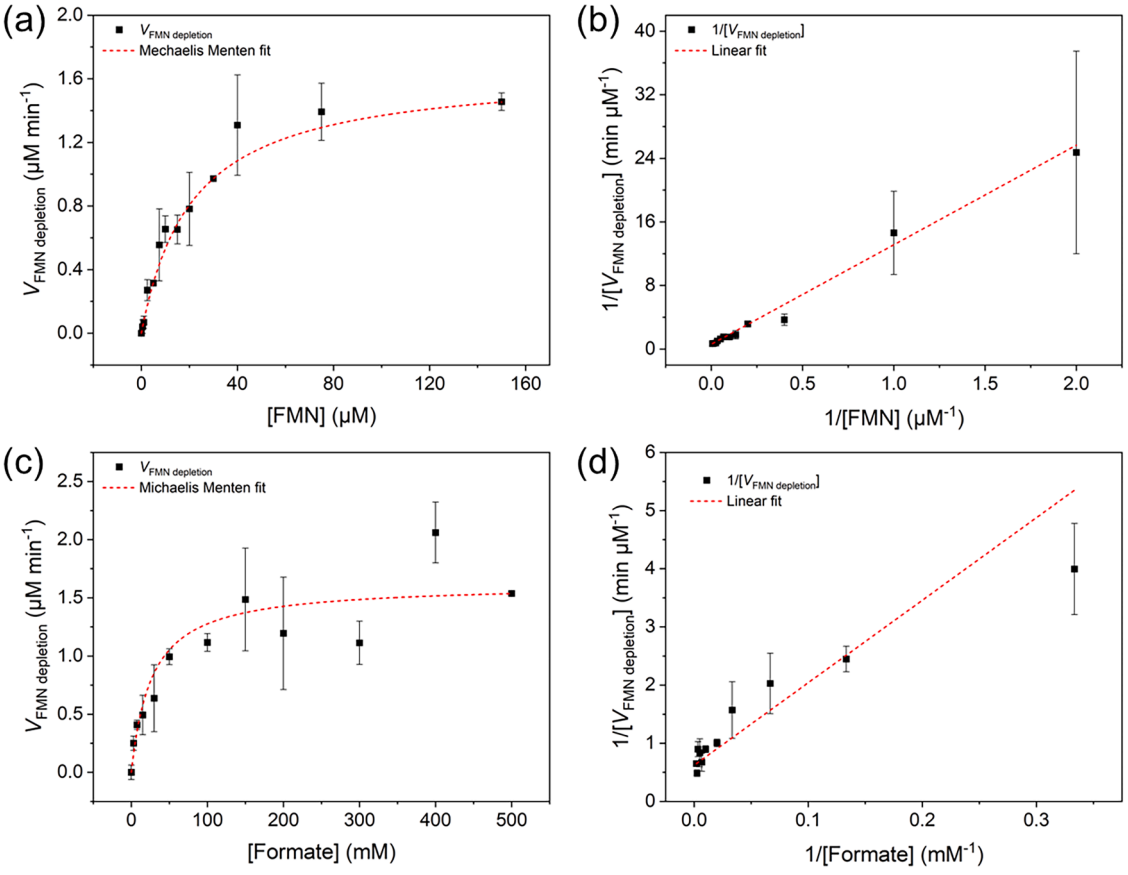

Fig. 4. Steady-state kinetic study of Rh@UiO-67. Michaelis-Menten fittings were performed against varying (a) FMN concentrations or (c) sodium formate concentrations. The formate and FMN concentrations were fixed at 300 mM and 50 μM, respectively. Lineweaver-Burk plots (b,d) were performed to verify the kinetic parameters. The assays were done in microplates in the glovebox at r.t. (20°C). Each well contains Rh@UiO-67 50 μM/mL in degassed Tris-HCl buffer (25 mM, pH 8.0). (PSE was performed using an added [Cp*Rh(BPyDC)Cl]Cl amount corresponding to 20 mol% of the original MOF's linker content).

Consequently, compared with the metal active center in Rh@UiO-67-Bpy, Cp*Rh in Rh@UiO-67 is more readily activated by hydrogen, whereas the subsequent hydrogen-donating step is less favorable. Given the overall lower activity of Rh@UiO-67 in trans-hydrogenation, the hydrogen-donating step is likely the rate-determining step.

Despite its lower activity, Rh@UiO-67 exhibited superior biocompatibility (vide infra), which led us to focus on Rh@UiO-67 rather than Rh@UiO-67-Bpy. The stability of rhodium incorporation during catalysis was further assessed by hot-filtration tests (Fig. S4): the reaction ceased immediately upon removal of Rh@UiO-67, demonstrating that the metal complex remained firmly coordinated within the framework and did not leach into solution. This stability not only sustains the catalytic activity of the complex but also minimizes potential enzyme inactivation by free rhodium species. Compared to its natural counterpart formate oxidase (FOx), Rh@UiO-67 exhibits higher stability against pH (4-9) and temperature (20-70°C) changes (Fig. S5).

Encouraged by these preliminary results, we investigated the kinetic parameters of the Rh@UiO-67-catalyzed reduction of FMN. Both the formation of the catalytically active hydrido-rhodium species and its subsequent re-oxidation by hydride transfer are thought to proceed via coordinative pre-equilibria, followed by a quasi-irreversible hydride transfer step to or from the rhodium center. Consequently, Michaelis-Menten type saturation kinetics were expected for both formate and FMN. Indeed, saturation behavior was observed for both substrates (Fig. 4). From the corresponding Lineweaver-Burk plots, K_M values of 20.5 ± 0.8 μM for FMN and 22.8 ± 3.4 mM for formate were determined, together with a kcat value of 20.2 ± 0.3 h^{-1} for the Rh catalyst. These values are remarkably similar to those previously reported for the soluble analogue $[Cp^*Rh(bpy)(H_2O)]^{2+}$ [17b] Notably, the K_M value for formate in this study is approximately three-fold lower than the earlier report. This difference, however, may reflect the lower buffer strength employed here, and thus reduce competition between formate and buffer for coordination to the rhodium center. In any case, it can be concluded that heterogenization of Cp*Rh did not adversely affect its catalytic performance.

3.3. Biocompatibility of Rh@UiOs

The central hypothesis of this work was that Cp*Rh immobilized on the UiO-67 framework is shielded to such an extent that interaction with high-molecular-weight ligands (i.e. enzymes) is either precluded or at least markedly slowed. Accordingly, our subsequent experiments focused on probing this interaction and the issue of mutual inactivation.

In an initial experiment, we compared the catalytic performance of Rh@UiO-67 and Rh@UiO-67-Bpy in the transfer hydrogenation of cyclohex-2-enone with formate, both in the presence and absence of bovine serum albumin (BSA). Somewhat unexpectedly, BSA exerted a pronounced effect on Rh@UiO-67-Bpy, reducing its catalytic activity by more than 80%. In contrast, Rh@UiO-67 appeared to be slightly activated in the presence of BSA (Fig. 5). As noted earlier, Rh@UiO-67-Bpy exhibits higher catalytic efficiency than Rh@UiO-67. A plausible explanation is that the larger surface area of Rh@UiO-67-Bpy exposes a greater fraction of rhodium active sites on the surface. While these surface-displayed sites are more readily accessible to substrates and thereby enhance activity, they are also more susceptible to interaction and deactivation by proteins. By contrast, Rh@UiO-67 provides a more balanced system, combining catalytic efficiency with protein compatibility. Protein compatibility is maintained even when the PSE ratio increases to 80%, as the crystallinity of UiO-67 framework is preserved (Fig. S6).

BSA is a typical globular protein (66.5 kDa) with a hydrodynamic radius of 33.7 Å [17] It is therefore far too large to efficiently penetrate the pores of UiO-67. Our biocatalyst of interest, the peroxygenase from *Agrocybe aegerita*, is somewhat smaller (51 kDa), although its hydrodynamic radius has not yet been determined [18] To probe size limitations, we performed a protein absorption test with homemade ladder including *Aae*UPO to evaluate enzyme accessibility to the Rh@UiO-67 pores (Fig. S7). During incubation, total protein concentration and protein composition in the supernatant barely changed, suggesting that negligible amount of protein was absorbed by Rh@UiO-67. A protein impurity slightly above 10 kDa was still shown on the SDS-PAGE after 7-hours incubation regardless of its low abundance, further confirming the size-exclusion capability of the Rh@UiO-67 framework.

Selected model proteins were employed to further examine the size-exclusive shielding of the Rh active site by the UiO-67 framework. We tested myoglobin (Mb, 17 kDa) and papain (23 kDa), which have a hydrodynamic radius of 9.7 Å and 18.4 Å, respectively (Fig. 7) [19] These are small proteins closer to the window size of UiO-67, yet the porous framework still prevented protein penetration. By contrast, small molecules such as amino acids were able to diffuse through the pores. When histidine was introduced, a pronounced loss of activity was observed for Rh@UiO-67. Nevertheless, Rh@UiO-67 retained nearly 30% of its activity, whereas the free Rh complex was completely deactivated, highlighting the protective effect of the MOF framework.

We then focused on the target cascade system to verify that immobilization of the Rh-complex suppresses its contact with *Aae*UPO and thereby prevents mutual deactivation (Fig. 7). Over an 8-hours period, no significant loss of activity was observed for either Rh@UiO-67 or

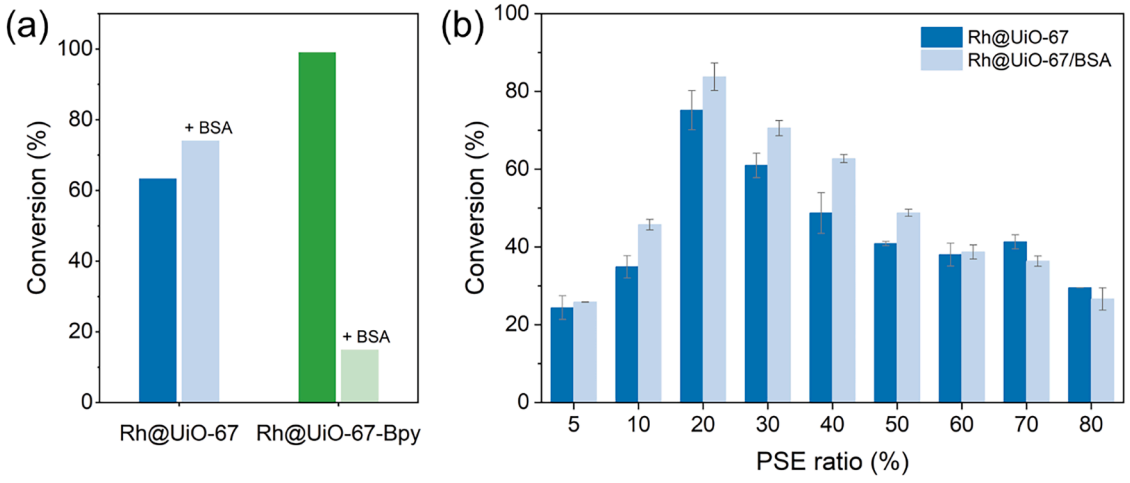

Fig. 5. (a) Cyclohexenone hydrogenation activity of Rh@UiO-67 and Rh@UiO-67-Bpy (PSE 20 mol%) with BSA as model protein. (b) Impact of PSE doping ratio on the protein compatibility of Rh@UiO-67. Reaction condition: formate 0.5 M, cyclohexenone 2 mM, Rh@UiO-67 or Rh@UiO-67-Bpy 2 mg/ml, BSA 0 or 10 mg/mL, reaction time 1 hour.

*Aae*UPO. Moreover, only negligible Rh activity was detected in the supernatant, indicating that the immobilization of the Rh active sites is robust under this condition. In comparison, incubation with the enzyme caused an immediate activity drop of free $[Cp^*Rh(BpyDC)Cl]^+$. While $[Cp^*Rh(BpyDC)Cl]^+$ also induced noticeable decrease in *Aae*UPO activity, complete deactivation was not observed due to the relatively low metal-enzyme (200:1) ratio applied [6].

3.4. Rh@UiO-67/FMN fueled peroxygenase reaction

The Rh@UiO-67/FMN system for in situ H_2O_2 generation was evaluated in the *Aae*UPO-catalyzed oxyfunctionalization of ethylbenzene as a model reaction. The cascade maintained high activity across pH 6-9, although an unexpected decrease was observed at pH 7. The highest overall cascade activity was observed at 40°C, while higher temperatures led to decreased activity (Fig. 6a-b). In biphasic systems using ethyl acetate as a substrate reservoir, the reaction proceeded approximately twice as fast as in monophasic buffer system.

The unexpected activity drop at pH 7 is noteworthy, given that both $[Cp^*Rh(bpy)]^{2+}$ complex [17b] and *Aae*UPO [20c] have been reported to perform optimally under near-neutral conditions. This suggests that factors such as enzyme-cofactor interactions or local microenvironment effects may influence cascade reaction. The optimum cascade activity at 40°C aligns with the typical temperature profile of *Aae*UPO, while further temperature increases led to reduced conversion, likely due to thermo-denaturation of the enzyme. The rapid loss of activity upon prolonged incubation indicates that thermal stress, exacerbated by mechanical agitation, accelerates enzyme inactivation. In contrast, Rh@UiO-67 is highly stable under these conditions. Compared to the monophasic system, the biphasic reaction system showed twofold increase in reaction rate, which is likely due to the alleviating of solubility limitations of hydrophobic substrates.Fig. 8

Under biphasic conditions, a scope of representative UPO substrates were tested using the in situ H_2O_2 generated by Rh@UiO-67/FMN (Table 2). *Aae*UPO-catalyzed hydroxylation, epoxidation and sulfoxidation were performed effectively. For the hydroxylation of ethylbenzene derivatives (*a-d*), corresponding (*R*)-alcohols were obtained with *ee* > 93%, indicating that the intrinsic enantioselectivity of *Aae*UPO was not influenced. Overoxidation to ketones remained under 10% in all cases except substrate *d*. The hydroxylation of cyclohexane is less efficient compared to the ethylbenzene substrates, as the phenyl position is more activated, yet still a TON of 9,413 was achieved. The highest TON (36,702) was observed in the epoxidation of *cis-β*-methyl styrene, giving (*1R,2S*)-*cis*-methyl styrene oxide in *ee* >99%. When using thioanisol as substrate, tandem system that uses free Cp*Ir complex to generate H_2O_2 gave low TON due to the inhibition of Cp*Ir catalytic center [6]. In this study, *Aae*UPO delivered a 21-fold TON of 29,081 in a 6-times shorter time frame using H_2O_2 in situ generated by Rh@UiO-67/FMN, consistent with the generally high efficiency of UPO-catalyzed oxyfunctionalization. Overall, the result supports that the shielding by UiO-67 framework stabilizes both the Rh center and the enzyme, enabling high activity in diverse reactions.

4. Conclusion

Cp*Rh incorporated to UiO-67 framework was employed as a transhydrogenation catalyst in the regeneration of $FMNH_2$, which subsequently generates H_2O_2 in situ for enzymatic oxyfunctionalization. The UiO-67 framework effectively shielded both transition metal and enzyme by spatial separation, mitigating the critical mutual deactivation in this tandem cascade. Using *Aae*UPO as a model peroxygenase, high activity and selectivity were maintained across a representative substrate scope. Compared with systems that generate H_2O_2 using homogeneous transition-metal catalysts, the Rh@UiO-67/FMN module delivered higher product concentrations in shorter reaction times. Moreover, the H_2O_2-generation unit showed greater operational stability than its natural counterpart *Ao*FOx, underscoring its potential as a H_2O_2-generation platform for diverse peroxide-dependent enzymatic cascades.

Supporting Information. Supplementary characterization methods and data are included in Supporting Information. The following files are available free of charge.

Enzyme production, GC analysis, Hot filtration reaction, and Supplementary characterizations (PDF)

Note

The manuscript was written through contributions of all authors. All authors have given approval to the final version of the manuscript.

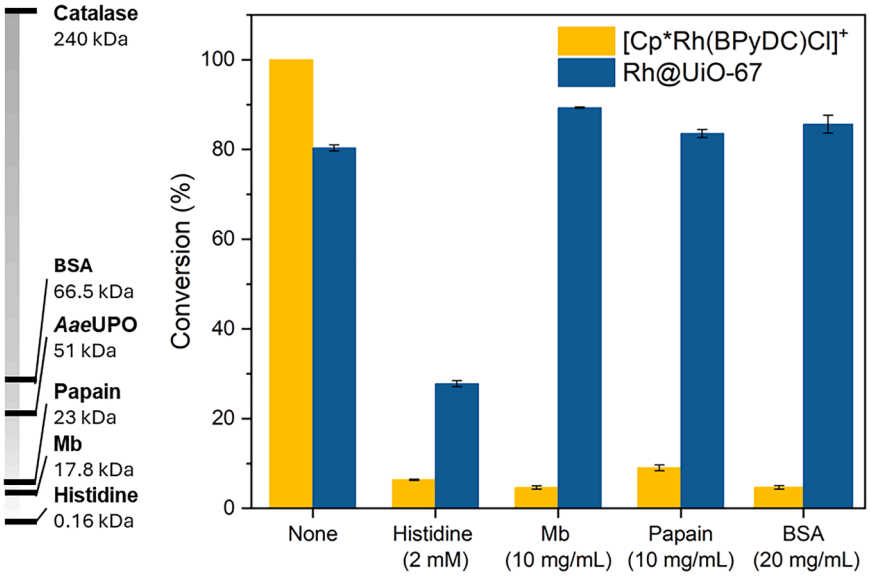

Fig. 6. Size-selective protection of Rh@UiO-67 against protein interference. The reactions in Tris-HCl buffer (50 mM, pH 8.0) contains formate 0.5 M, cyclohex-2-enone 2 mM, Rh@UiO-67 2 mg/mL or [Cp*Rh(BPyDC)Cl]Cl 1.1 mM, and the interfere proteins. The reactions were performed at 40°C, 800 rpm. Reactions time 2 hours.

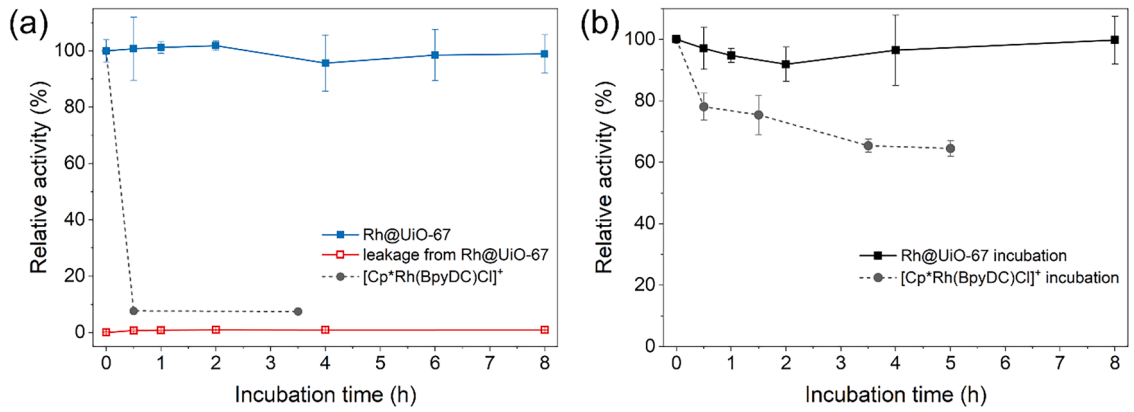

Fig. 7. Rh@UiO-67 and *Aae*UPO activity monitored during one-pot incubation. (a) Activity of incubated Rh@UiO-67 and residual activity in the supernatant. (b) *Aae*UPO activity in the supernatant after incubation. 1 μM of UPO was incubated with 2 mg/mL Rh@UiO-67 or $[Cp^*Rh(BpyDC)Cl]^+$ (0.5 mM in A and 0.2 mM in B). Rh activity was determined by transfer hydrogenation of 2 mM cyclohex-2-enone in Tris-HCl buffer (25 mM, pH 8.0) contains 0.5 M formate. UPO activity was determined by ABTS assay.

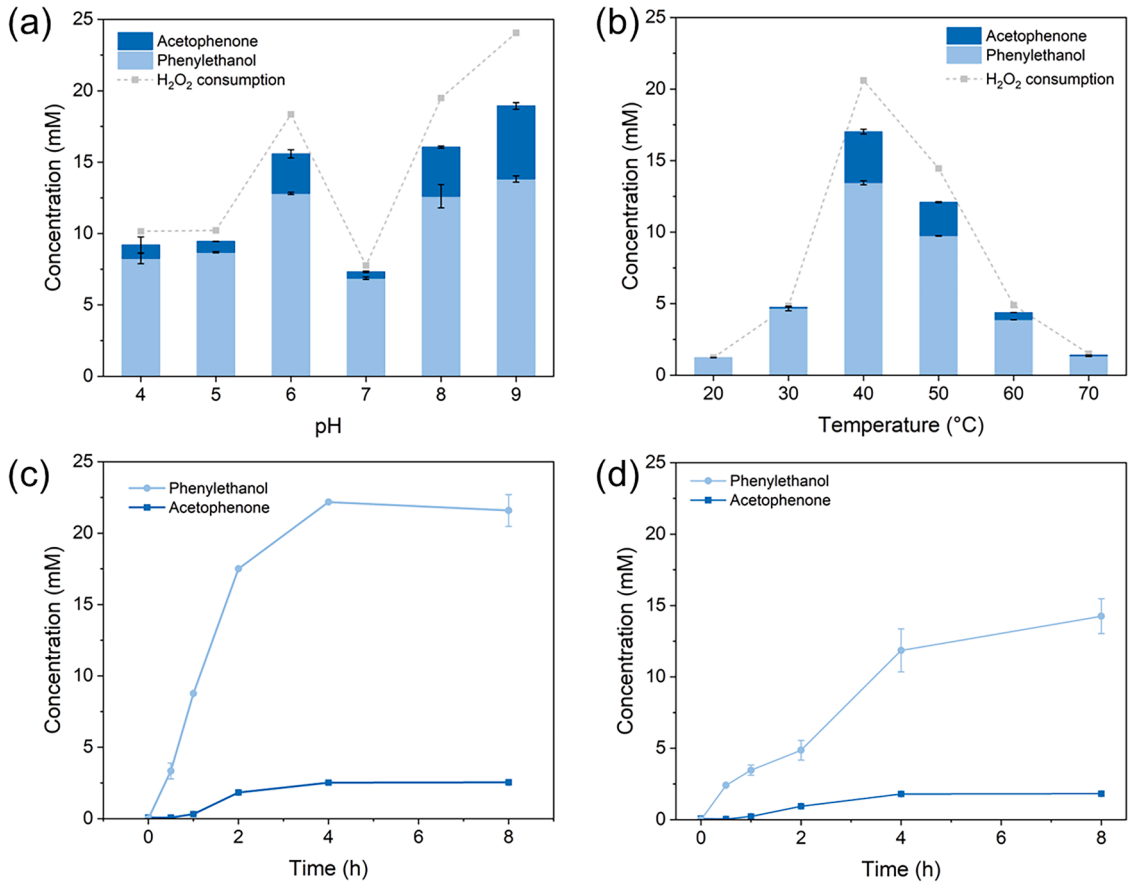

Fig. 8. Tandem reaction optimization of Rh@UiO-67/FMN-*Aae*UPO in the ethylbenzene oxyfunctionalization. Different (a) pH and (b) temperatures were tested in the monophasic cascade. Time course of the (c) biphasic and (d) monophase reactions were recorded at pH 8, 40°C. Each reaction contains formate 0.4 M, FMN 4 mM, *Aae*UPO 1 μM, and Rh@UiO-67 2 mg/mL (PSE 20 mol%). Ethylbenzene 20 mM with ACN (4% v/v) for monophasic system, or 100 mM in EtOAc for biphasic system. Reactions under pH 4-5 were performed in acetate buffer (25 mM), while pH 6-9 in Tris-HCl buffer (25 mM). 800 rpm, 4 hours.

Abbreviations

Cp*, Pentamethylcyclopentadienyl; Bpy, Bipyridyl; MOF, Metal-organic framework; FMN, Flavin mononucleotide, PSE, Post-synthetic exchange; *Aae*UPO, Unspecific peroxygenase from *Agrocybe aegerita;* *Ao*FOx, Formate oxidase from *Aspergillus oryzae*; BSA, Bovine serum albumin; Mb, myoglobin; ACN, acetonitrile; EtOAc, Ethyl acetate.

CRediT authorship contribution statement

Yutong Wang: Writing – original draft, Investigation, Data curation, Conceptualization. **Chunyu Huang:** Investigation. **Jelco Albertsma:** Investigation. **Monique van der Veen:** Supervision. **Miguel Alcalde:** Supervision. **Frank Hollmann:** Writing – review & editing, Supervision, Funding acquisition, Conceptualization.

Table 2
Oxyfunctionalization of substrates ***a-g*** by Rh@UiO-67/FMN-*Aae*UPO tandem.

	Substrate	Product **1** (mM)		Product **2** (mM)		*ee* **1** (%)	TON_{AaeUPO}
a			18.6 ± 0.2		2.5 ± 0.3	98 *(R)*	23630
b	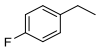	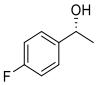	9.3 ± 0.7	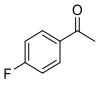	0.05 ± 0.07	97 *(R)*	9352
c	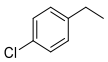	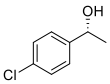	18.0 ± 0.1	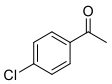	2.5 ± 0.03	93 *(R)*	23011
d		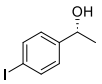	17.8 ± 0.2	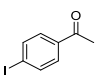	4.7 ± 1.6	98 *(R)*	27149
e			8.3 ± 1.2		0.6 ± 0.2	n.d.	9413
f			36.7 ± 0.3			99 *(1R,2S)*	36702
g			29.1 ± 1.3			n.d.	29081

Reaction condition: biphasic system consists of EtOAc (10 % v/v) in Tris-HCl buffer 25 mM pH 8.0; [sodium formate]=0.4 M, [substrate]=100 mM, [*Aae*UPO]=1 μM, [Rh@UiO-67]=2 mg/mL (PSE 20 mol%), [FMN]=4 mM, 40°C, 800 rpm. Data is expressed as the mean ± SD of the two independent experiments performed in duplicates.

Declaration of competing interest

The authors declare the following financial interests/personal relationships which may be considered as potential competing interests:

Given his role as editor, Frank Hollmann had no involvement in the peer review of this article and had no access to information regarding its peer review. Full responsibility for the editorial process for this article was delegated to another journal editor. If there are other authors, they declare that they have no known competing financial interests or personal relationships that could have appeared to influence the work reported in this paper.

Acknowledgement

This research was funded by the European Union (ERC, PeroxyZyme, No 101054658). Views and opinions expressed are however those of the authors only and do not necessarily reflect those of the European Union or the European Research Council. Neither the European Union nor the granting authority can be held responsible for them.

Supplementary materials

Supplementary material associated with this article can be found, in the online version, at doi:10.1016/j.mcat.2026.115702.

Data availability

Data will be made available on request.

References

[1] (a) U. Kölle, M. Grätzel, Organometallic Rhodium(III)Complexes as Catalysts for the Photoreduction of Protons to Hydrogen on Colloidal TiO2, Angew. Chem. Int. Ed. 26 (1987) 567–570;
(b) D. Westerhausen, S. Herrmann, W. Hummel, E. Steckhan, Formate-Driven, Nonenzymatic NAD(P)H Regeneration for the Alcohol-Dehydrogenase Catalyzed Stereoselective Reduction of 4-Phenyl-2-Butanone, Angew. Chem.-Int. Edit. Engl. 31 (1992) 1529–1531;
(c) E. Steckhan, S. Herrmann, R. Ruppert, J. Thommes, C. Wandrey, Continuous Generation of NADH from NAD+ and Formate Using a Homogeneous Catalyst with Enhanced Molecular-Weight in a Membrane Reactor, Angew. Chem.-Int. Edit. Engl. 29 (1990) 388–390;
(d) R. Ruppert, S. Herrmann, E. Steckhan, Efficient indirect electrochemical in-situ regeneration of NADH:electrochemically driven enzymatic reduction of pyruvate catalyzed by D-LDH, Tetraherdon Lett 28 (1987) 6583–6586.
[2] F. Hollmann, B. Witholt, A. Schmid, [Cp*Rh(bpy)(H2O)]2+: a versatile tool for efficient and non-enzymatic regeneration of nicotinamide and flavin coenzymes, J. Mol. Catal. B: Enzym. 19-20 (2002) 167–176.
[3] F. Hollmann, A. Schmid, Towards [Cp*Rh(bpy)(H2O)]2+-promoted P450 catalysis: Direct regeneration of CytC, J. Inorg. Biochem. 103 (2009) 313–315.
[4] R. Ruppert, S. Herrmann, E. Steckhan, Very Efficient Reduction of NAD(P)+ with Formate Catalyzed by Cationic Rhodium Complexes, J. Chem. Soc.-Chem. Commun. (1988) 1150–1151.
[5] M.Mifsud Grau, M. Poizat, I.W.C.E. Arends, F. Hollmann, Phosphite-driven regeneration of reduced enzyme cofactors, Appl. Organometal. Chem. 24 (2010) 380–385.
[6] C. Domestici, Y. Wu, T. Hilberath, M. Alcalde, F. Hollmann, A. Macchioni, Hybrid Organometallic and Enzymatic Tandem Catalysis for Oxyfunctionalisation Reactions, ChemCatChem 15 (2023) e202201623.
[7] M. Poizat, I.W.C.E. Arends, F. Hollmann, On the nature of mutual interaction between [Cp*Rh(bpy)(H2O)]2+ and enzymes – analysis and potential remedies, J. Mol. Catal. B. Enzym. 63 (2010) 149–156.
[8] F. Hildebrand, S. Lütz, Stable Electroenzymatic Processes by Catalyst Separation, Chem. Eur. J. 15 (2009) 4998–5001.
[9] (a) Y. Okamoto, V. Köhler, C.E. Paul, F. Hollmann, T.R. Ward, Efficient In Situ Regeneration of NADH Mimics by an Artificial Metalloenzyme, ACS Catalysis 6 (2016) 3553–3557;

(b) V. Köhler, M.Durrenberger Y.M.Wilson, D. Ghislieri, E. Churakova, T. Quinto, L. Knorr, D. Haussinger, F. Hollmann, N.J. Turner, T.R. Ward, Synthetic cascades are enabled by combining biocatalysts with artificial metalloenzymes, Nat. Chem. 5 (2013) 93–99.

[10] Y.M. Wilson, M. Durrenberger, E.S. Nogueira, T.R. Ward, Neutralizing the detrimental effect of glutathione on precious metal catalysts, J Am Chem Soc 136 (2014) 8928–8932.

[11] T. Himiyama, M. Waki, Y. Maegawa, S. Inagaki, Cooperative Catalysis of an Alcohol Dehydrogenase and Rhodium-Modified Periodic Mesoporous Organosilica, Angew Chem Int Ed Engl 58 (2019) 9150–9154.

[12] (a) Y. Zhang, B. Wei, H. Liang, Rhodium-Based MOF-on-MOF Difunctional Core-Shell Nanoreactor for NAD(P)H Regeneration and Enzyme Directed Immobilization, ACS Appl Mater Interfaces 15 (2023) 3442–3454;
(b) Y. Wu, J. Shi, D. Li, S. Zhang, B. Gu, Q. Qiu, Y. Sun, Y. Zhang, Z. Cai, Z. Jiang, Synergy of Electron Transfer and Electron Utilization via Metal–Organic Frameworks as an Electron Buffer Tank for Nicotinamide Regeneration, ACS Catalysis 10 (2020) 2894–2905.

[13] A.H. Vahabi, F. Norouzi, E. Sheibani, M. Rahimi-Nasrabadi, Functionalized Zr-UiO-67 metal-organic frameworks: Structural landscape and application, Coordination Chemistry Reviews (2021) 445.

[14] (a) M.J. Katz, Z.J. Brown, Y.J. Colon, P.W. Siu, K.A. Scheidt, R.Q. Snurr, J. T. Hupp, O.K. Farha, A facile synthesis of UiO-66, UiO-67 and their derivatives, Chem Commun (Camb) 49 (2013) 9449–9451;
(b) J.H. Cavka, S. Jakobsen, U. Olsbye, N. Guillou, C. Lamberti, S. Bordiga, K. P. Lillerud, A New Zirconium Inorganic Building Brick Forming Metal Organic Frameworks with Exceptional Stability, Journal of the American Chemical Society 130 (2008) 13850–13851.

[15] (a) Y. Benseghir, A. Lemarchand, M. Duguet, P. Mialane, M. Gomez-Mingot, C. Roch-Marchal, T. Pino, M.H. Ha-Thi, M. Haouas, M. Fontecave, A. Dolbecq, C. Sassoye, C. Mellot-Draznieks, Co-immobilization of a Rh Catalyst and a Keggin Polyoxometalate in the UiO-67 Zr-Based Metal-Organic Framework: In Depth Structural Characterization and Photocatalytic Properties for CO_2 Reduction, J Am Chem Soc 142 (2020) 9428–9438;
(b) M.B. Chambers, X. Wang, N. Elgrishi, C.H. Hendon, A. Walsh, J. Bonnefoy, J. Canivet, E.A. Quadrelli, D. Farrusseng, C. Mellot-Draznieks, M. Fontecave, Photocatalytic carbon dioxide reduction with rhodium-based catalysts in solution and heterogenized within metal-organic frameworks, ChemSusChem 8 (2015) 603–608.

[16] F.G. Cirujano, F.X. Llabrés i Xamena, Tuning the Catalytic Properties of UiO-66 Metal–Organic Frameworks: From Lewis to Defect-Induced Brønsted Acidity, The Journal of Physical Chemistry Letters 11 (2020) 4879–4890.

[17] M.A. Ank Valstar, Wyn Brown, The Interaction of Bovine Serum Albumin with Surfactants Studied by Light Scattering, Langmuir 16 (2000) 922–927.

[18] (a) R. Ullrich, M. Hofrichter, The haloperoxidase of the agaric fungus Agrocybe aegerita hydroxylates toluene and naphthalene, FEBS Lett 579 (2005) 6247–6250;
(b) F. Tonin, F. Tieves, S. Willot, A. van Troost, R. van Oosten, S. Breestraat, S. van Pelt, M. Alcalde, F. Hollmann, Pilot-Scale Production of Peroxygenase from Agrocybe aegerita, Org Process Res Dev 25 (2021) 1414–1418;
(c) P. Molina-Espeja, E. Garcia-Ruiz, D. Gonzalez-Perez, R. Ullrich, M. Hofrichter, M. Alcalde, Directed evolution of unspecific peroxygenase from Agrocybe aegerita, Appl Environ Microbiol 80 (2014) 3496–3507;
(d) P. Molina-Espeja, S. Ma, D.M. Mate, R. Ludwig, M. Alcalde, Tandem-yeast expression system for engineering and producing unspecific peroxygenase, Enzyme and Microbial Technology 73-74 (2015) 29–33.

[19] (a) M.T. Naoki Baden, Intermolecular Interaction of Myoglobin with Water Molecules along the pH Denaturation Curve, J. Phys. Chem. B 110 (2006) 15548–15555;
(b) M.T. Jungkwon Choi, Denaturation of a Protein Monitored by Diffusion Coefficients: Myoglobin, J. Phys. Chem. B 106 (2002) 6587–6593;
(c) S. Bhaswati, C. Apala, D. Nilimesh, S. Pratik, Single Molecular Level Probing of Structure and Dynamics of Papain Under Denaturation, Protein & Peptide Letters 24 (2017) 1073–1081.